Magnetization Vector Rotation Reservoir Computing Operated by Redox Mechanism

Wataru Namiki[†], *Daiki Nishioka*[†,‡], *Takashi Tsuchiya*[*,†], *Tohru Higuchi*[‡], *and Kazuya Terabe*[†]

[†]Research Center for Materials Nanoarchitectonics, National Institute for Materials Science, 1-1 Namiki, Tsukuba, Ibaraki 305-0044, Japan

[‡]Department of Applied Physics, Faculty of Science, Tokyo University of Science, 6-3-1 Niijuku, Katsushika, Tokyo 125-8585, Japan

KEYWORDS. Reservoir computing, Magnetic property tuning, Planar Hall effect, Redox, solid-state electrolyte, Lithium ion

Physical reservoir computing is a promising way to develop an efficient artificial intelligence using physical devices exhibiting nonlinear dynamics. Although magnetic materials have advantages in miniaturization, the need for a magnetic field results in high electric power consumption and a complex device structure. To resolve these issues, we propose a redox-based physical reservoir utilizing the planar Hall effect and anisotropic magnetoresistance, which are phenomena described by different nonlinear functions of the magnetization vector, that does not need a magnetic field to be applied to it. The expressive power of this reservoir network based on an all-solid-state redox

transistor occupying a small volume is higher than that of previous reservoir networks. The normalized mean square error of the reservoir on a benchmark task was 1.69×10^{-3}, which is lower than that of a memristor array (3.13×10^{-3}) even though the number of reservoir nodes was fewer than half that of the memristor array.

Reservoir computing has attracted attention as a promising way of implementing an efficient artificial intelligence that can process time-series data.[1-3] This sort of computing has advantages in terms of its learning cost due to its fewer learning parameters than in conventional deep learning and its ability to mimic biological systems.[4,5] These advantages could be used to reduce the amount of information traffic, since the majority of information would be pre-processed on the physical reservoir. Candidates for the physical reservoir include electrical circuits, electrochemical elements, magnetic devices, optical elements, robotic system, ion-gating devices, and so on.[6-43] They all share three key features, i.e., nonlinear transformation, short-term memory, and the ability to map time-series data to a higher dimensional space. In particular, the magnetic devices (i.e., spin torque oscillators, spin wave homogeneous media, anisotropic magnetoresistance arrays, and so on) have shown high computational performance in spoken-digit recognition and time series-data prediction tasks in addition to being excellent candidates for miniaturization, reaching sub-μm^2 scales.[13-28,41] So far however, physical reservoirs made from magnetic materials have needed a magnetic field to be applied to them, which leads to the fatal problems of high electrical power consumption and structural complexity. Thus, to reduce electric power consumption and simplify the device structure, it is necessary to find a magnetic physical reservoir that does not require a magnetic field to be applied.

Here, we focused on using an ion-gating reservoir (IGR) that utilizes the transient responses of ions in an electrolyte and ions and electronic carriers in a channel.[38,39] The complex response of this miniaturized device gives high expressive power to the reservoir, leading to high computation power. Recently, we reported that the magnetization properties (i.e., magnetization amplitude, magnetoresistance, and magnetization direction) of magnetite thin film in an all-solid-state redox device can be dramatically manipulated with the redox (reduction/oxidization) mechanism at room temperature[44,45] and indicated that an ion-gating technique can be used to manipulate not only electrical but also magnetic properties. This technique does not need a magnetic field to be applied since the magnetization vector $\boldsymbol{M}$ is determined by the electronic carrier density, which can be easily tuned by the redox reaction together with the application of a low voltage (2.0 V). The modulation of $\boldsymbol{M}$ can be tracked by the planar Hall effect whose electric motive force depends on the amplitude and direction of the magnetizations and anisotropic magnetoresistance.[46-49] Thus, it is possible to acquire information on $\boldsymbol{M}$ from the electric signal. Although there are some reports on neuromorphic devices utilizing electrical conductivity modulation in a magnetite thin film, there is no reported neuromorphic application capable of modulating both the direction and amplitude of the magnetization.[50,51]

In this letter, we demonstrate reservoir computing utilizing information on $\boldsymbol{M}$ obtained from an all-solid-state redox device, named a magnetic vector rotation reservoir. The magnetite thin film used as the channel layer incorporates Li ions into the crystal lattice with a finite relaxation time.[44,45] The electronic carriers are doped by charge compensation and contribute to the modulation of $\boldsymbol{M}$. Thus, the planar Hall effect and anisotropic magnetoresistance response, which are based on $\boldsymbol{M}$, can be used as a physical reservoir that does not require a magnetic field to be applied to it. We found that this magnetization vector rotation reservoir outperformed a 90-node memristor array (normalized mean square error, NSME, of 1.69×10^{-3} versus NMSE of 3.13×10^{-3}) in a task of solving a second-order nonlinear dynamic equation even though it had a smaller network (40 nodes).[8]

The magnetization rotation reservoir device is schematically shown in Figure 1a. The device was fabricated as follows. Magnetite thin film was deposited on a MgO (110) single crystal in order to give it uniaxial magnetic anisotropy.[45,52,53] Raman spectroscopy (Figure 1b) confirmed that the film contained no other iron oxide impurities (e.g., FeO, Fe_2O_3). The film area was 500×700 μm^2. Electrodes with a hall-bar shape were deposited on the film. The electrical current electrode was aligned to the 110 direction of the MgO substrate. Prior to depositing the Au gate electrode, Li_2O-ZrO_2-SiO_2 (LZSO) thin film, an Li^+-conductive electrolyte, was deposited. A high-resolution transmission electron microscope (HR-TEM) image of a cross-section of the device is shown in Figure 1c. Fast Fourier transforms (FFTs) for the substrate and the thin film regions are also shown. These images confirm that the magnetite thin film grew epitaxially and coherently on the MgO (110) single crystal. Figure1d shows the magnetoresistance (MR) in the magnetite thin film at magnetic fields ranging from -14 T to 14 T. The negative MR curve, which the previous study also observed, reflects how the spin polarized current at the grain boundary varies under various magnetic fields.[44] The relative MR variation is in good agreement with previous reports, indicating that the fabricated thin film had comparable properties to the films used in the previous studies.[44,54] Here, φ is defined as the relative angle between the drain current vector $\boldsymbol{I}_D$ and the magnetization vector $\boldsymbol{M}$. The transverse voltage V_{xy} and longitudinal voltage V_{xx} reflect the planar Hall signal detected at the V+(xy) and V-(xy) terminals and the potential drop detected at the V+(xx) and V-(xx) terminals, respectively. As shown in Figures 1e and f, V_{XY} and V_{XX} of the magnetite thin film depend on φ as follows:[48,49]

$$V_{XY} = I_D(R_{\|}-R_{\perp})/2 \sin2\varphi = M^2k/\mathrm{t} \sin2\varphi \quad (1)$$

$$V_{XX} = I_D R_{\perp} + I_D(R_{\|}-R_{\perp})\cos^2\varphi = I_D R_{\perp} + 2M^2k/\mathrm{t} \cos^2\varphi \quad (2),$$

where $R_{\|}$ and $R_{\perp}$ respectively denote the electrical resistance for magnetic fields perpendicular and parallel to I_D. k and t are constants relating to anisotropic magnetoresistance and film thickness, respectively. From equations 1 and 2, it can be seen that both V_{XY} and V_{XX} reflect the direction and amplitude of the magnetization, but they exhibit different electronic carrier tuning behaviors since the nonlinear function of the V_{XY} signal against φ differs from the V_{XX} one. Figure 1g plots normalized I_D curves for gate voltages (V_G) swept at various rates. It shows that, as the sweep rate increased, I_D described a smaller hysteresis. This modulation results from electronic carrier doping induced by the Li ions in the magnetite thin film, as shown in Figure 1h. The redox reaction is as follows,

$$Fe_3O_4 + x\mathrm{Li}^+ + xe^- \leftrightarrow \mathrm{Li}_xFe_3O_4 \quad (3)$$

and

$$\mathrm{Fe}^{3+}{}_{16d} + \mathrm{Fe}^{2+}{}_{16d} + \mathrm{Fe}^{3+}{}_{8a} + xe^-$$

$$\leftrightarrow (1-x)\mathrm{Fe}^{3+}{}_{16d} + (1+x)\mathrm{Fe}^{2+}{}_{16d} + \mathrm{Fe}^{3+}{}_{8a} \quad (4).$$

Here, 16d and 8a mean octahedral sites and tetrahedral sites. The observed modulation rate of ~19 % is in good agreement at the rate found in the previous study (~20 %).[45] Area of hysteresis in the density variation of the doped electronic carriers and the time dependence of the amount of doped electronic carriers could be controlled by varying the application time and/or sweeping speed of V_G. In addition, the amplitude and direction of the magnetization can be manipulated by tuning the electronic carrier density.[44,45] The Li ions are at 16c sites, which are vacant octahedra with an oxygen at each corner.[55] To maintain charge neutrality, a spin-down dopant electron occupies the Fe_{16d} site. This electron not only helps to tune the electronic carrier density; it also decreases M and rotates it.[44,45] Note that V_{XX}

shows not only anisotropic magnetoresistance but also electrical conductivity modulations, whose rates are < 3 % for anisotropic magnetoresistance and 20 % for electrical conductivity.[44] Since V_{XY} and V_{XX} have information on $\boldsymbol{M}$ and the superimposition of $\boldsymbol{M}$ and the electrical conductivity, complex nonlinear behavior can be obtained by tuning the electronic carriers (see the inset of Figure 1g).

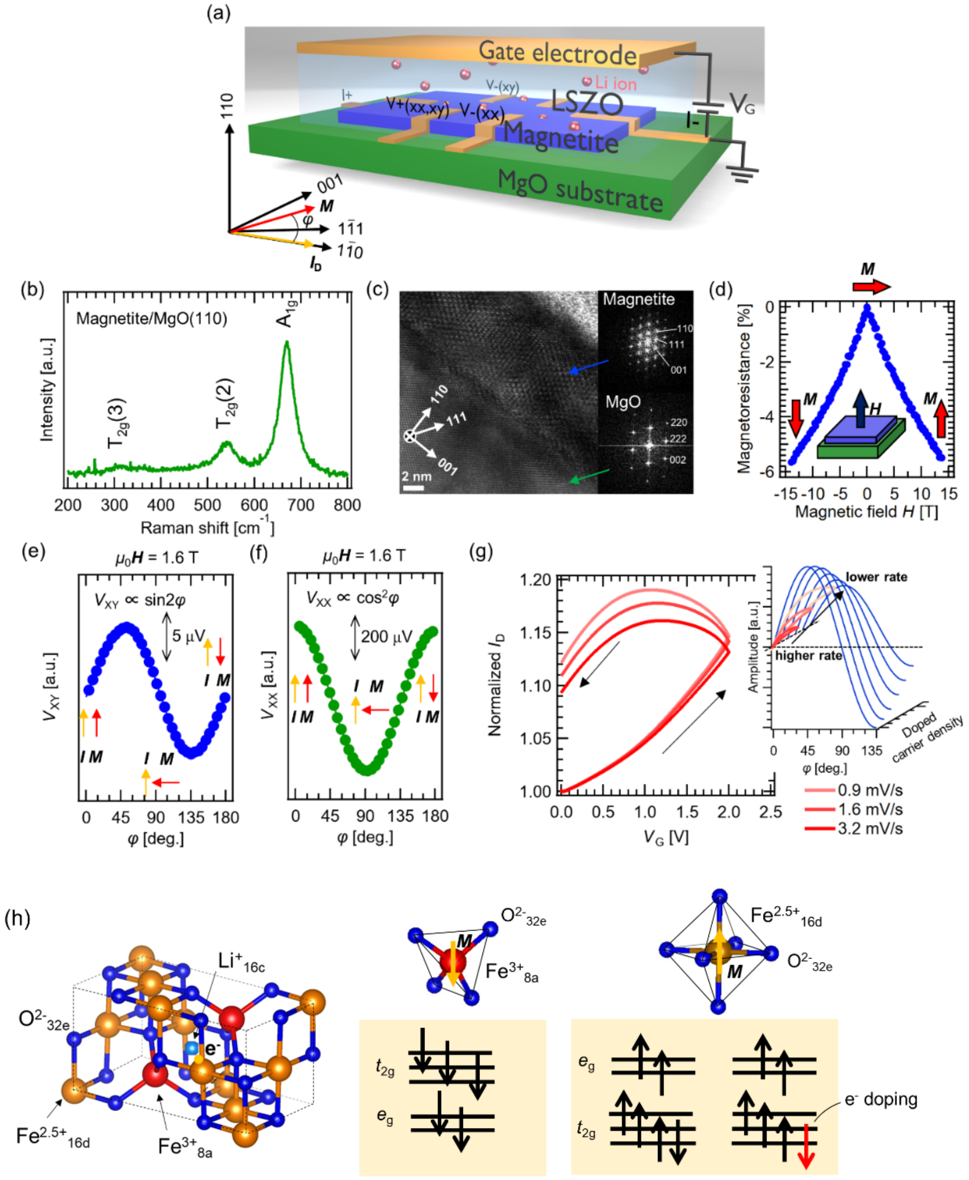

Figure 1. (a) Schematic illustration of magnetization vector rotator reservoir device. φ is defined as the relative angle between the electric current I_D and magnetization $\boldsymbol{M}$. (b) Raman spectrum of a magnetite/MgO substrate structure. (c) TEM image of a cross-section of the device and its fast Fourier transform. (d) Magnetic field dependence of magnetresistance of the magnetite thin film under a magnetic field applied perpenducular to the film surface. (e) Plot of V_{XY} versus the magnetization vector φ. (f) Plot of V_{XX} versus φ. A magnetic field of 1.6 T was applied during the measurements. (g) I_D response against V_G swept at various rates. Inset: Variation in I_D at different sweep rates with magnetization rotation associated with carrier doping. Blue and red solid lines show the variation in signal amplitude depending on magneitzation rotation and varition in I_D, respectively. (h) Schematic illustration of electron donation in a magnetite cell and spin configuration of Fe ion at tetrahedral site and octahedral site. The red arrow denotes the spin-down state.

The reservoir computing model is illustrated in Figure 2a. The model consists of an input layer, a reservoir, and output layers connected by weight parameters (i.e., input weights W_{in} and output weights W_{out}). Since W_{in} and the weights (W) connecting each node in the reservoir layer are fixed, the only learning parameter in this model is W_{out}. The reservoir in the network is a physical device. Its dimensionality was increased by utilizing two responses, i.e., V_{XY} corresponding to magnetization modulation and V_{XX} corresponding to anisotropic magnetoresistance modulation. The idea is that, when a series of pulsed voltages with a fixed pulse period is input to the gate electrode, V_{XY} and V_{XX} exhibit different waveforms depending on the electronic carrier tuning. Each pulse period corresponds to a time step k. The response of V_{XY} to an input pulsed voltage with a discrete time step is shown in Figure 2b. Twenty node states, labeled $X_1(k)$-$X_{20}(k)$, are taken from the waveform per time step k, which corresponds to one pulse period. Figure 2c shows the dependence of each X_i on k, where i is the node number. It can be seen that the waveforms of the node states have various shapes, indicating that the reservoir has high expressive power. Figure 2d shows the case of another 20 node states, $X_{21}(k)$-$X_{40}(k)$, taken from the waveform of V_{XX}. In this case as well, the dependence of X_i varies with k (Figure 2e). The output of the reservoir network $y(k)$ can be expressed in terms of $X_1(k)$ to $X_{40}(k)$, as follows:

$$y(k) = \sum_{i=1}^{40} W_i X_i \qquad (5).$$

Here, W_i denotes the i-th output weight connecting the reservoir and the output layers in the network.

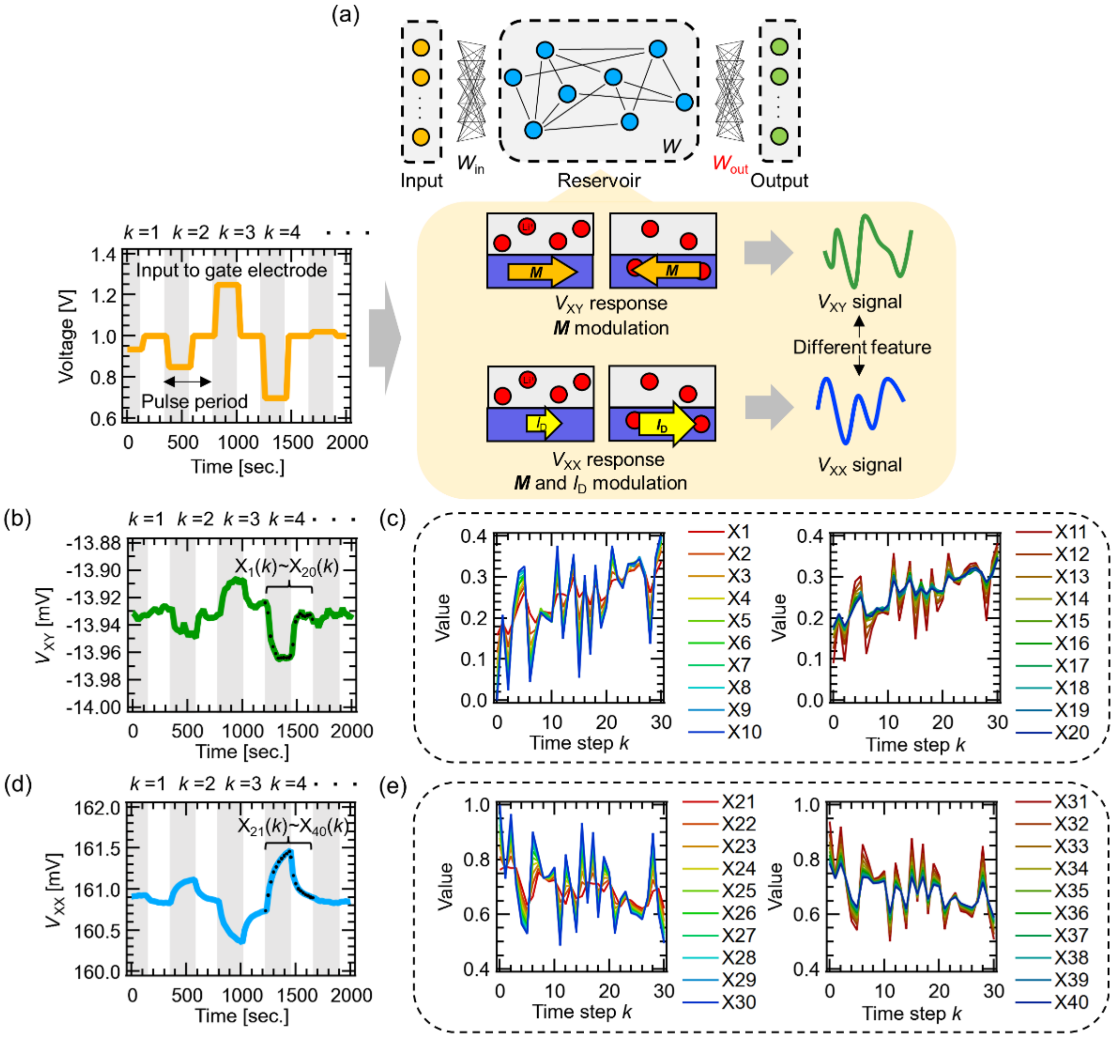

Figure 2. (a) Concept of reservoir computing utilizing a magnetization vector rotation reservoir and schematic illustration of V_{XY} and V_{XX} responses to a pulsed voltage. (b) Cropped V_{XY} response for the input pulsed voltage with a discrete time step. (c) Dependence of 20 node states, X_1-X_{20}, on k. (d) Cropped V_{XX} response for input pulsed voltage with a discrete time step. (e) Dependence of 20 node states, (X_{21}-X_{40}_on k.

Figure 3a shows the process flow diagram of the second-order nonlinear system prediction task, [8,14,37-39]

$$d(k) = 0.4d(k-1) + 0.4d(k-1)d(k-2) + 0.6u^3(k) + 0.1 \qquad (6),$$

in which $d(k)$ denotes the output of the system for an input $u(k)$at k. To perform this task with high accuracy, the physical reservoir must have excellent nonlinearity, the ability to map time-series data to a high dimensional space, and a short-term memory because equation (6) includes a nonlinear term and a term based on the past state.[8] The original random input data were transformed into a pulse voltage train [0.5 V, 1.5 V] with a base level of V_G = 1.0 V. The pulse period ranged from 50 to 200 seconds. The learning parameter W_i was optimized to minimize the error between output and target waveforms in the training phase, and the optimized value was used in the test phase. Figures 3b-f compare the waveforms predicted in the training and test phases. The output waveforms are in good agreement with the target waveforms. The prediction error, which is defined as NMSE, for various pulse periods is summarized in Figure 3g. NMSE decreases as pulse period expands. The minimum NMSE was 1.69×10^{-3} in a pulse period of 150 seconds. This value is much smaller than that of a 90 memristor array (NMSE: 3.13×10^{-3}) even though the network had only 40 nodes.[8] This result shows that giving V_{XY} and V_{XX} different nonlinear responses improves the expressive power of the reservoir relative to that of an array of devices with similar responses.

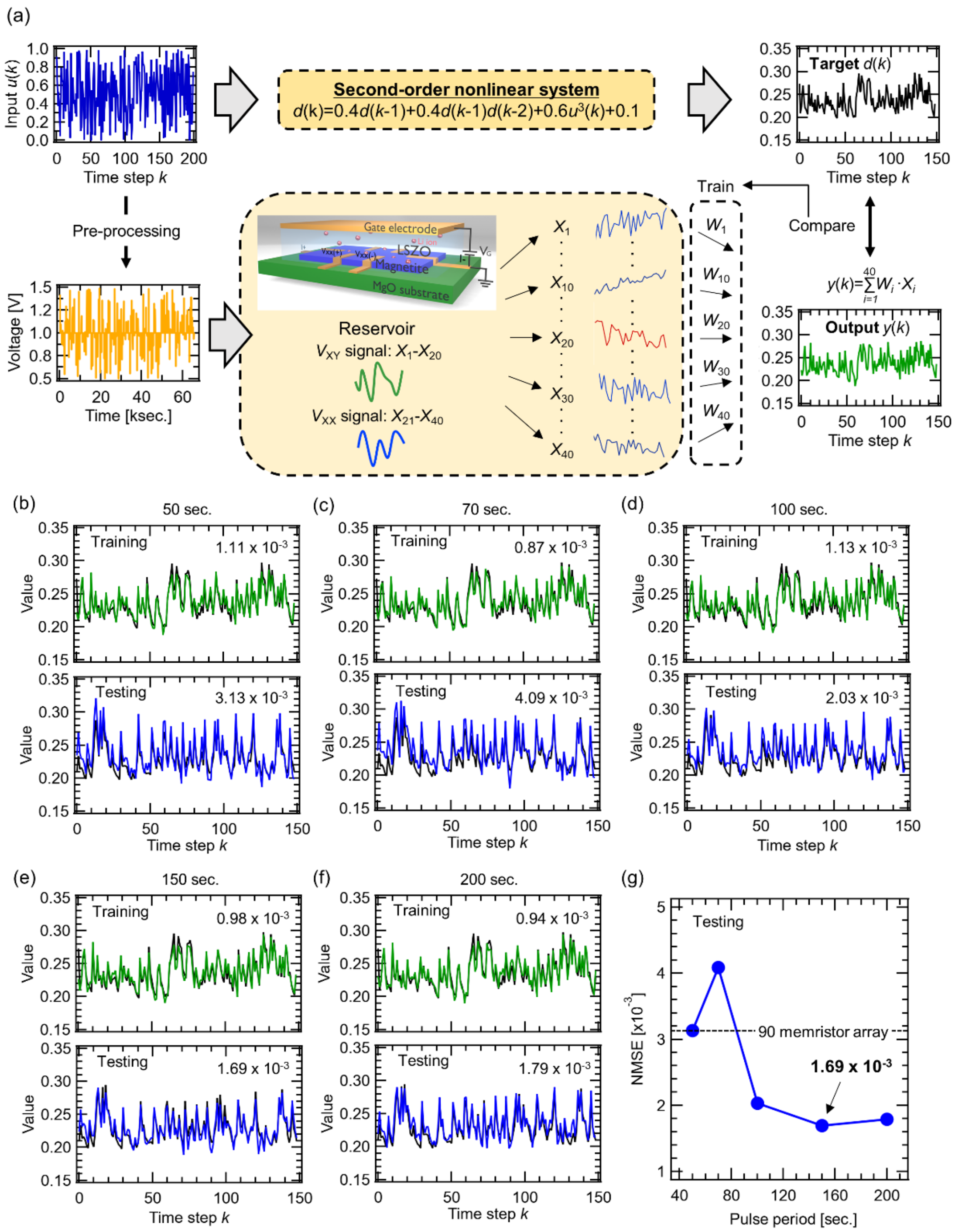

Figure 3. (a) Using a magnetization vector rotation reservoir to process time-series data. (b)-(f) Predictions in the training phase and testing phase of a second-order nonlinear system for pulse periods of 50, 75, 100, 150, and 200 seconds. The black, green, and blue lines denote the target and

prediction results of the training and testing phases. (g) NMSE at various pulse intervals. The dashed solid line denotes the NMSE of a 90-memristor array.[8]

To determine the reasons for the improvement in performance relative to the previous study, we evaluated the memory capacity (MC) of the physical reservoir device. Figures 4a-e show the dependence of the coefficient of determination r^2 (i.e., forgetting curve) on the step delay in various pulse periods. r^2 maintains a value above 0.5 by approximately a step delay of 2, indicating the value 2 steps before can be reproduced with high accuracy. Figure 4f shows the change in MC in various pulse periods. Here, MC is defined as the area surrounding the forgetting curve and is an indicator of the short-term memory. The maximum MC (3.97) is for a pulse period of 150 seconds, which corresponds to the condition with the minimum NMSE. This may be a reason for the improvement. Another factor could be nonlinearity; here, we compared the output signals for different pulsed V_G inputs. Figure 4g shows the normalized V_{XY} at one k. For all pulse periods, V_{XY} responds nonlinearly to the input pulse. The rise and fall of the V_{XY} outputs within the normalized time interval from pulse-on to -off become steeper as the input pulse period becomes longer, whereas those before this normalized time becomes smaller. To evaluate the nonlinearity of the $\boldsymbol{M}$ rotation induced by V_G, we used the correlation coefficient r to evaluate the nonlinearity of the M rotation induced by V_G, because it is a measure of the nonlinearity of the V_{XY} response. Figure 4h replots the responses of V_{XY} at one k shown in Figure 4g. One cycle of the plots reflects various V_{XY} responses in one pulse period. If the response is linear, the plots should follow the dashed line in the figure. Apparently, the responses do not follow the dashed line and thus show nonlinear behavior. It can be seen that hysteresis area expands as the pulse period increases. This result shows that the nonlinearity becomes stronger as the pulse period expands. To evaluate the nonlinearity, we used the correlation coefficient r as an indicator:

$$r = \frac{\frac{1}{n}\sum_{i=1}^{n}(a_i - \bar{a})(b_i - \bar{b})}{\sqrt{\frac{1}{n}\sum_{i=1}^{n}(a_i - \bar{a})^2}\sqrt{\frac{1}{n}\sum_{i=1}^{n}(b_i - \bar{b})^2}} \quad (7).$$

Here, n, a, b, $\bar{a}$, and $\bar{b}$ are the number of data, the value of V_{XY}, the value of the linear line, the average of a, and the average of b, respectively. The corresponding plot in Figure 4i shows that the values of r at pulse-on and pulse-off are slightly different, which in turn indicates that the response of V_{XY} in one pulse period shows asymmetric nonlinear behavior. r decreases as the pulse period increases. This result shows that the V_{XY} response shows strong nonlinearity when the electronic carrier density is higher (i.e., the pulse period is longer). Figures 4j and k are schematic illustrations of the V_{XY} response based on $M^2\sin2\varphi$ under a pulse voltage. $\boldsymbol{M}$ rotates counterclockwise (i.e., φ decreases) and its amplitude increases (Figure 4j) during the pulse-on period. On the other hand, $\boldsymbol{M}$ rotates clockwise (i.e., φ increases) and the amplitude decreases during the pulse-off period (voltage is 1.0 V) (Figure 4k). V_{XY} has a strong nonlinear response both in its direction and amplitude to the $\boldsymbol{M}$ modulation induced by V_G.

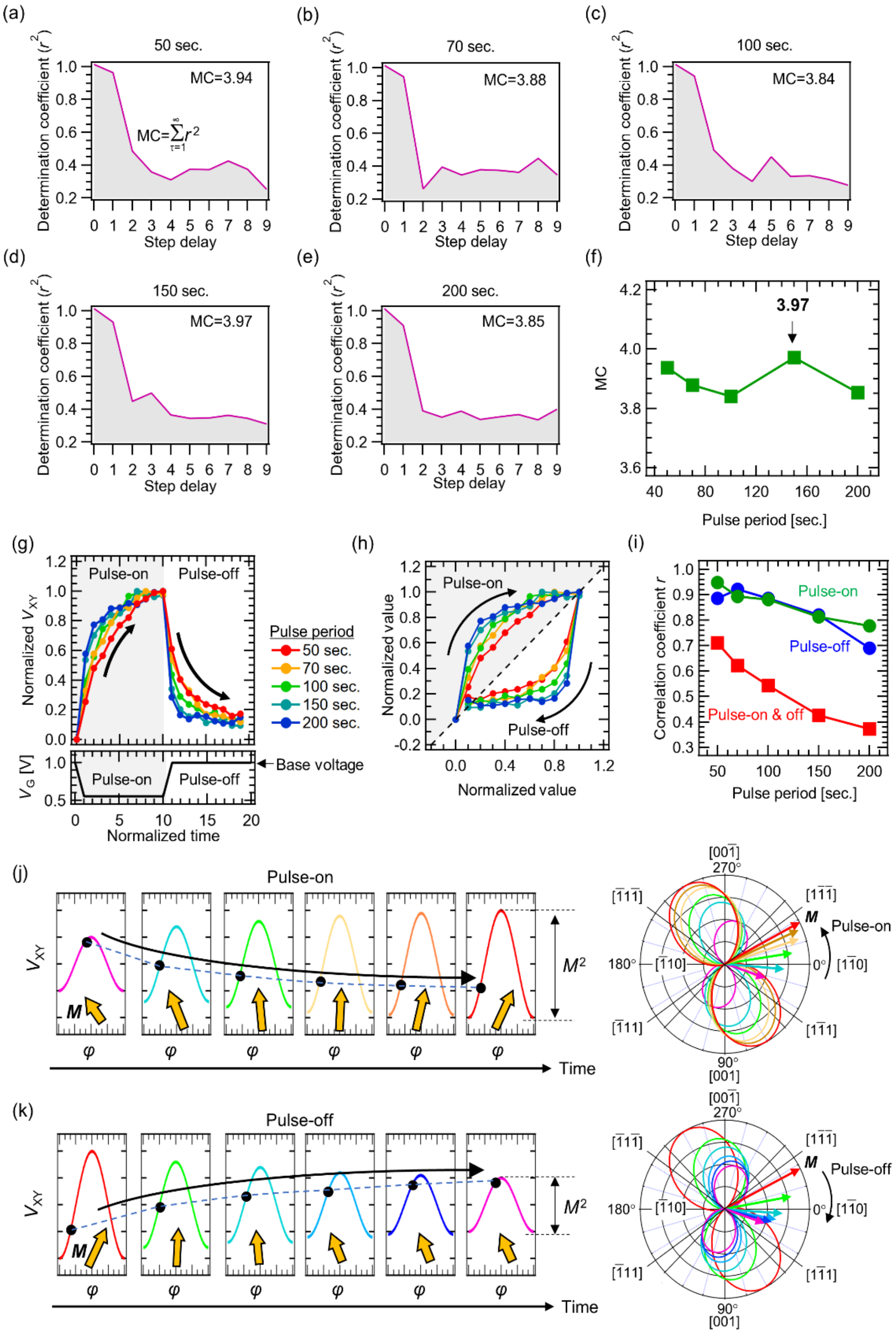

Figure 4. (a)-(e) Forgetting curves, which show the dependence of the determination coefficient on the step delay, for pulse periods of 50, 75, 100, 150, and 200 seconds. (f) Memory capacity in various pulse periods. (g) Normalized V_{XY} response for pulse inputs with various periods. The time axis is

normalized to correspond to one time step k. (h) Replotted V_{XY} response at one k. (i) Correlation coefficient variation of V_{XY} response in various pulse periods. (j) Schematic illustrations of V_{XY} response based on $M^2\sin2\varphi$ (left) and magnetic anisotropy and magnetization vector (right) during the pulse-on period. (k) Schematic illustrations of V_{XY} response based on $M^2\sin2\varphi$ (left) and magnetic anisotropy and magnetization vector (right) during the pulse-off period.

In summary, we demonstrated a magnetization rotation reservoir that exhibits two nonlinear responses, V_{XY} and V_{XX}, to the modulation of the magnetization $\boldsymbol{M}$ of reservoir's magnetite thin film without application of a magnetic field at room temperature. While V_{XY} purely depends on $\boldsymbol{M}$, V_{XX} depends on the anisotropic magnetoresistance and electrical conductivity. It was found that varying the electronic carrier density as a means of modulating $\boldsymbol{M}$ gives the physical reservoir excellent nonlinearity characteristics and helped it to outperform an array consisting of a single kind of memristors.[8] The principle of the magnetization rotation reservoir is not limited to magnetite thin film; it can be applied to other ferromagnetic metallic and semiconducting materials. This development will improve the versatility of physical reservoir computing thanks to its low electric power consumption, excellent miniaturization prospects, and simple device structure.

Fabrication of Magnetization Vector Rotation Reservoir Device. A magnetization vector rotation reservoir device was fabricated on the flat surface of a MgO (110) substrate.[45] A 12-nm-thick, 500 × 700 μm² magnetite channel layer was deposited by pulsed laser deposition (PLD) using a magnetite polycrystalline target. The base pressure in the deposition chamber was 3.3×10^{-5} Pa. The substrate temperature was kept at 573 K during deposition, and the laser repetition rate was 5 Hz.

The flow rate of the Ar (99 %) and O_2 (1%) mixture gas was fixed at 0.2 sccm, and the pressure was kept at 1.3×10^{-3} Pa. A 5-nm-thick Ti adhesion layer and 50-nm-thick Pt electrode with a Hall-bar shape were continuously deposited on the magnetite thin film by rf magnetron sputtering. A Li_2O-ZrO_2-SiO_2 (LZSO) thin film was deposited by PLD, using a Li-excess LZSO ceramic target, in a 3.4 Pa O_2 atmosphere at a flow rate of 8.5 sccm. Finally, the Au gate electrode was deposited on the LSZO electrolyte by rf magnetron sputtering. Metal shadow masks were used to pattern each layer.

Evaluation of fabricated device. The quality of the deposited magnetite thin film was evaluated with micro-Raman spectroscopy. The wavelength of the incident light was 573 nm, and the power was set at 0.5 mW to avoid thermal oxidation. The exposure time and integration number were set to 120 seconds and 20 times. As for the dependence of V_{XX} and V_{XY} of the magnetite thin film on the magnetization angle φ, the current vector was aligned to <110> and the drain current I_D was set to 7 μA. The V_{XX} and V_{XY} signals were measured using nanovolt meters with the magnetic field of 1.6 T rotating clockwise. The resulting V_{XX} and V_{XY} curves showed no distortion since φ equaled the angle through which the magnetic field vector rotated. The conductivity of the Li ions in the LZSO of the fabricated device was measured with a Solartron SI-1260 frequency response analyzer. Electrical measurements (i.e., plotting the I_D curve by sweeping V_G and measuring the V_{XX} and V_{XY} responses to input pulse gate voltage (V_G)) were performed on the device in a vacuum by using a Keithley 4200-SCS parameter analyzer.

Voltage measurement of voltage response for random V_G pulse input. To obtain the V_{XX} and V_{XY} responses to random time-series data, the data were transformed into pulsed voltage data. Five pulse trains with different pulse periods (50, 75, 100, 150, and 200 seconds) were prepared in order to optimize the input conditions. Here, V_{XX} and V_{XY} were voltage signals reflecting the electrical resistance and planar Hall effect. Each pulse train had a base voltage of 1.0 V and an amplitude range of [0.5, 1.5 V]. Five pulse trains were input one by one with time intervals in between. V_G during each interval was 1.0 V. Prior to measuring the V_{XX} and V_{XY} responses to V_G, the magnetization was saturated parallel to the easy direction <111> on the 110 plane by using a permanent magnet with a magnetic field of 450 mT. Then, the magnetic field was removed, and I_D was set to 2 μA during the measurement.

Nonlinear time series data prediction task. The original input data were transformed into pulsed voltages. One pulse period corresponded to one discrete time step *k*. The response signal was output from a physical device, and the node state X_i was sampled from the signal. Since the magnetization vector rotation reservoir of this study output two responses (i.e., V_{XX} and V_{XY}), 40 nodes could be used for computing by obtaining 20 node states from each response. These 40 node states were connected by using the output weight matrix $\boldsymbol{W}_{\mathrm{out}}$, to generate the reservoir output *y*. $\boldsymbol{W}_{\mathrm{out}}$ was optimized in the training phase by minimizing the difference between the target waveform output $d(n)$ of the theoretical model and the reservoir output $y(k)$. $y(k)$ is described as

$$y(k) = \sum_{\boldsymbol{i=1}}^{\boldsymbol{n}} W_i X_i(k) + b. \quad (8)$$

Here, *n*, W_i, and *b* are the total number of nodes, an element of $\boldsymbol{W}_{\mathrm{out}}$, and a bias term, respectively. W_i was optimized by ridge regression. The test phase evaluated the performance of the network. W_{out} optimized in the training phase was used in the test phase as is. The number of time step *k* used in the training and test phases was 150, since the first 50 time steps in each phase were discarded. To compare the performance of the reservoir system with that of other systems, the errors were calculated by using the normalized mean square error (NMSE) defined as follows,

$$\mathrm{NMSE} = \sum_{k=1}^{T} \frac{(d(k)-y(k))^2}{(d(k))^2}. \quad (9)$$

Here, T, $d(k)$, and $y(k)$ are the lengths in the training phase ($T = 150$) or test phase ($T = 150$), the target signal, and the predicted signal.

Ridge regression for solving second-order nonlinear dynamic equation. The readout network of the magnetization rotation reservoir was trained by ridge regression for time-series data analysis. In this ridge regression, the reservoir output $y(k)$ shown in equation 8 is transformed to

$$y(k) = \boldsymbol{W}_{\mathrm{out}} \cdot \boldsymbol{X}(k) \qquad (10).$$

Here, $\boldsymbol{W} = (w_0, w_1, \ldots, w_n)$ and $\boldsymbol{X}(k) = (X_0(k), X_1(k), \ldots, X_n(k))^{\mathrm{T}}$ are the weight vector and the reservoir state vector for a reservoir of size n, respectively. Note that $w_0 = \mathrm{b}$ and $\mathrm{X}_0(k) = 1$ to introduce the bias b shown in equation 8. The cost function $J(\boldsymbol{W})$ of the ridge regression is defined as

$$J(W) = \frac{1}{2}\sum_{k=1}^{T}(y_t(k) - y(k))^2 + \frac{\beta}{2}\sum_{i=0}^{N} w_i{}^2 \qquad (11),$$

where T, β, and $y_t(k)$ are the data length in the training phase, the ridge parameter, and the target output generated by equation 6, respectively. We set $T = 150$ and $\beta = 5\times10^{-4}$. The weight matrix $\widehat{\boldsymbol{W}}$, which minimizes the cost function $J(\boldsymbol{W})$, is given by the following equation:

$$\widehat{\boldsymbol{W}} = \boldsymbol{Y}\boldsymbol{X}^T(\boldsymbol{X}\boldsymbol{X}^T + \lambda\boldsymbol{I})^{-1} \qquad (12).$$

Here, $\boldsymbol{Y} = (y_t(1), y_t(2), \ldots, y_t(T))$, $\boldsymbol{X}(k) = (X(1), X(2), \ldots, X(T))$, and $\boldsymbol{I}(\subseteq \mathbb{R}^{(N+1)\times(N+1)})$ are the target output vector, the reservoir state matrix, and the identity matrix, respectively. The computational performance of the task was evaluated by computing NMSE after the readout weight was learned.

Estimation of short-term memory capacity. A delay task was performed to determine whether the system could recover past input data as current input. $u(k)$ is applied to the magnetization rotation reservoir and the input $u(k\text{-}\tau)$ before the delay time τ is reconstructed by a linear combination of reservoir states and W obtained from the current response of the reservoir. The square of the correlation coefficient between the ideal target $u(k\text{-}\tau)$ and the model predictions $y(k)$ was determined by utilizing the relationship,

$$r^2(\tau) = \frac{Cov^2(d(k),y(k,\tau))}{Var(d(k))\times Var(y(k,\tau))}, \quad (13)$$

where Cov(A, B) is the covariance between vectors A and B, and Var(A) ≅ Cov(A, A). r^2 takes values between 0 and 1, where 1 indicates perfect replication of the targets. The short-term memory capacity C_{STM} was calculated by taking the sum of the $r^2(\tau)$ values over the range of delays, i.e.,

$$C_{STM} = \sum_{k=1}^{\infty} r^2\,(\tau). \quad (14)$$

AUTHOR INFORMATION

Corresponding Author

*Takashi Tsuchiya
TSUCHIYA.Takashi@nims.go.jp

Author Contributions

W.N., D.N., T.T., and K.T. conceived the idea for the study. W.N. designed the experiments. W.N. and T.T. wrote the paper. W.N. prepared the samples. W.N. carried out the experiments. W.N., D.N., and T.T. analyzed the data. All authors discussed the results and commented on the manuscript. K.T. directed the projects.

ACKNOWLEDGMENT

This work was supported in part by the Japan Society for the Promotion of Science (JSPS), KAKENHI Grant numbers, JP22H04625 (Grant-in-Aid for Scientific Research on Innovative Areas “Interface Ionics”) and JP21J21982 (Grant-in-Aid for JSPS Fellows). Part of this work was supported by the Iketani Science and Technology Foundation. Part of this work was supported by the Electron microcopy unit of the National Institute for Materials Science.

REFERENCES

1. Jaeger, H.; Haas, H. Harnessing Nonlinearity: Predicting Chaotic Systems and Saving Energy in Wireless Communication. *Science* **2004**, *304*, 78-80.
2. Maass, W.; Natschläger, T.; Markram, H. Real-Time Computing without Stable States: A New Framework for Neural Computation based on Perturbations. *Neural Comput.* **2002**, *14*, 2531-2560.
3. Verstraeten, D.; Schrauwen, B.; D'Haene, M.; Stroobandt, D. An Experimental Unification of Reservoir Computing Methods. *Neural Networks* **2007**, *20*, 391-403.
4. Stepny, S. The Neglected Pillar of Material Computation. *Physica D: Nonlinaer Phenom.* **2008**, *237*, 1157-1164.
5. Dale, M.; Miller, J. F.; Stepney, S.; Trefzer M. A. A Substrate-Independent Framework to Characterize Reservoir Computers. *Proc. R. Soc. A* **2019**, *475*, 20180723.
6. Appeltant, L.; Sorano, M. C.; van der Sande, G.; Danckaert, J.; Massar, S.; Dambre, J.; Schrauwen, B.; Mirasso, C. R.; Fischer, I. Information Processing using a Single Dynamical Node as Complex System. *Nat. Commun.* **2011**, *2*, 468.
7. Appeltant, L.; van der Sande, G.; Danckaert, J.; Fischer, I. Constructing Optimized Binary Masks for Reservoir Computing with Delay Systems. *Sci. Rep.* **2014**, *4*, 3629.
8. Du, C.; Cai, F.; Zidan, M. A.; Ma, W.; Lee, S. H.; Lu, W. D. Reservoir Computing using Dynamics Memristors for Temporal Information Processing. *Nat. Commun.* **2017**, *8*, 2204.
9. Midya, R.; Wang, A.; Asapu, S.; Zhang, X.; Rao, M.; Song, W.; Zhuo, Y.; Upadhyay, N.; Xia, Q.; Yang, J. J. Reservoir Computing using Diffusive Memristors. *Adv. Intel. Sys.* **2019**, *1*, 1900084.
10. Kan, S.; Nakajima, K.; Asai, T.; Kasaya, M. A. Physical Implementation of Reservoir Computing through Electrochemical Reaction. *Adv. Sci.* **2022**, *9*, 2104076.
11. Kan, S.; Nakajima, K.; Asai, T.; Kasaya, M. A. Simple Reservoir Capitalizing on the Nonlinear Response of Materials: Theory and Physical Implementations. *Phys. Rev. Appl.* **2021**, *15*, 024030.
12. Kasaya, M. A.; Takeshima, Y.; Kan, S.; Nakajima, K.; Oya, T.; Asai, T. Performance of Reservoir Computing in a Random Network of Single-walled Carbon Nanotubes Complexed with Polyoxometalate. *Neuromorph. Comput. and Eng.* **2022**, *2*, 014003.
13. Torrejon, J.; Riou, M.; Araujo, F. A.; Tsunegi, S.; Khalsa, G.; Querlioa, D.; Bortolotti, P.; Cros, V.; Yakushiji, K.; Fukushima, A.; Kubota, H.; Yuasa, S.; Stiles, M. D.; Grollier, J. Neuromorphic computing with nanoscale spintronic oscillators. *Nature*, **2017**, *547*, 428.
14. Jiang, W.; Chen, L.; Zhou, K.; Li, L.; Fu, Q.; Du, Y.; Liu, R. H. Physical Reservoir Computing using Magnetic Skyrmion Memristor and Spin Torque Nano-oscillator. *Appl. Phys. Lett.* **2019**, *115*, 192403.
15. Akashi, N.; Yamaguchi, T.; Tsunegi, S.; Taniguchi, T.; Nishida, M.; Sakurai, R.; Wakao, Y.; Nakajima, K. Input-driven Bifurcations and Information Processing Capacity in Spintronics Reservoirs. *Phys. Rev. Res.* **2020**, *2*, 043303.
16. Kanao, T.; Suto, H.; Mizushima, K.; Goto, H.; Tanamoto, T.; Nagasawa, T. Reservoir Computing on Spin-torque Oscillator Array. *Phys. Rev. Appl.* **2019**, *12*, 024052.

17. Tsunegi, S.; Taniguchi, T.; Nakajima, K.; Miwa, S.; Yakushiji, K.; Fukushima, A.; Yuasa, S.; Kubota, H. Physical Reservoir Computing based on Spin Torque Oscillator with Forced Synchronization. *Appl. Phys. Lett.* **2019**, *114*, 164101.

18. Taniguchi, T.; Ogihara, A.; Utsumi, Y.; Tsunegi, S. Spintronic Reservoir Computing without Driving Current or Magnetic Field. *Sci. Rep.* **2022**, *12*, 10627.

19. Nakane, R.; Tanaka, G.; Hirose, A. Reservoir Computing with Spin Waves Excited in a Garnet Film. *IEEE Access* **2018**, *6*, 4462-4469.

20. Nakane, R.; Hirose, A.; Tanaka, G. Spin Waves Propagating through a Stripe Magnetic Domain Structure and Their Applications to Reservoir Computing. *Phys. Rev. Res.* **2021**, *3*, 033243.

21. Ichimura, T.; Nakane, R.; Tanaka, G.; Hirose, A. A Numerical Exploration of Signal Detector Arrangement in a Spin-wave Reservoir Computing Device. *IEEE Access* **2021**, *9*, 72637.

22. Nakane, R.; Hirose, A.; Tanaka, G. Performance Enhancement of a Spin-wave-based Reservoir Computing System Utilizing Different Physical Conditions. *Phys. Rev. Appl.* **2023**, *19*, 034047.

23. Papp, A.; Csaba, G.; Porod, W. Characterization of Nonlinear Spin-wave Interference by Reservoir-computing Metrics. *Appl. Phys. Lett.* **2021**, *119*, 112403.

24. Watt, S.; Kostylev, M.; Ustinov, A. B. Enhancing Computational Performance of a Spin-wave Reservoir Computer with Input Synchronization. *J. Appl. Phys.* **2021**, *129*, 044902.

25. Watt, S.; Kostylev, M. Reservoir Computing Using a Spin-wave Delay-line Active-ring Resonator Based on Yttrium-iron-garnet Film. *Phys. Rev. Appl.* **2020**, *13*, 034057.

26. Watt, S.; Kostylev, M.; Ustinov, A. B.; Kalinikos, B. A. Implementing a Magnonic Reservoir Computer Model Based on Time-delay Multiplexing. *Phys. Rev. Appl.* **2021**, *15*, 064060.

27. Namiki, W.; Nishioka, D.; Yamaguchi Y.; Tsuchiya, T.; Higuchi, T.; Terabe K. Experimental Demonstration of High-performance Physical Reservoir Computing with Nonlinear Interfered Spin Wave Multi-detection. *arXiv* **2022**, 2207.03216.

28. Vidamour, I. T.; Swindells, C.; Venkat, G.; Fry, P. W.; Welbourne, A.; Rowan-Robinson, R. M.; Backes, D.; Maccherozzi, F.; Dhesi, S. S.; Vasilaki, E.; Allwood, D. A.; Hayward, T. J. Reservoir Computing with Emerging Dynamics in a Magnetic Metameterial. *arXiv* **2022**, 2206.04446.

29. Nakajima, M.; Tanaka, K.; Hashimoto, T. Scalable Reservoir Computing on Coherent Linear Photonic Processor. *Commun. Phys.* **2021**, *4*, 20.

30. Sunada, S.; Uchida, A. Photonic Reservoir Computing Based on Nonlinear Wave Dynamics at Microscale. *Sci. Rep.* **2019**, *9*, 19078.

31. Okumura, T.; Tai, M.; Ando, M. Experimental Study on Parallel and Analog Optical Reservoir Computing with Delayed Feedback System for Physical Implementation. *Nonlinear Theory Appl.* **2019**, *10*, 236-248.

32. Paquot, Y.; Duport, F.; Smerieri, A.; Dambre, J.; Schrauwen, B.; Haelterman, M.; Massar, S. Optoelectronic Reservoir Computing. *Sci. Rep.* **2012**, *2*, 287.

33. Duport, F.; Smerieri, A.; Akrout, A.; Haelterman, M.; Massar, S. Fully Analogue Photonic Reservoir Computer. *Sci. Rep.* **2016**, *6*, 22381.

34. Vinckier, Q.; Duport, F.; Smerieri, A.; Vandoorne, K.; Bienstman, P.; Haelterman, M.; Massar, S. High-performance Photonic Reservoir Computer Based on a Coherently Driven Passive Cavity. *Optica* **2015**, *2*, 438-446.

35. Hermans, M.; Antonik, P.; Haelterman, M.; Massar, S. Embodiment of Learning in Electro-optical Signal Processors. *Phys. Rev. Lett.* **2016**, *117*, 128301.

36. Nakajima, K.; Hauser, H.; Li, T.; Pfeifer, R. Information Processing via Physical Soft Body. *Sci. Rep.* **2015**, *5*, 10487.

37. Koh, S. G.; Shima, H.; Naitoh, Y.; Akinaga, H.; Kinoshita, K. Reservoir Computing with Dielectric Relaxation at an Electrode-ionic Liquid Interface. *Sci. Rep.* **2022**, *12*, 6958.

38. Nishioka, D.; Tsuchiya, T.; Namiki, W.; Takayanagi, M.; Imura, M.; Koide, Y.; Higuchi, T.; Terabe, K. Edge-of-chaos Learning Achieved by Ion-electron-coupled Dynamics in an Ion-gating Reservoir. *Sci. Adv.* **2022**, *8*, eade1156.

39. Wada, T.; Nishioka, D.; Namiki, W.; Tsuchiya, T.; Higuchi, T.; Terabe, K. A Redox-based Ion-gating Reservoir Utilizing Double Reservoir States in Drain and Gate Nonlinear Responses. *Adv. Intell. Syst.* **2023**, 2300123.

40. Brazani, B.; Dion, G.; Morissette, J.-F.; Beaudoin, L.; Sylvestre, J. Microfabricated Neuroaccelerometer: Integrating Sensing and Reservoir Computing in MEMS. *J. Microelectromech. Sys.* **2020**, *29*, 338-347.

41. Gartside, J. C.; Stenning, G. D.; Vanstone, A.; Holder, H. H.; Arroo, D. M.; Dion, T.; Caravelli, F.; Kurebayashi, H.; Branford, W. R. Reconfigurable Training and Reservoir Computing in an Artificial Spin-vortex Ice via Spin-wave Fingerprinting. *Nat. Nanotech.* **2022**, *17*, 460.

42. Fuller, E. J.; Gabaly, F. E.; Léonard, F.; Agarwal, S.; Plimpton, S. J.; Jacobs-Gedrim, R. B.; James, C. D.; Marinella, M. J.; Talin, A. A. Li-Ion Synaptic Transistor for Low Power Analog Computing. *Adv. Mater.* **2017**, 29, 1604310.

43. Yang, C.-S.; Shang, D.-S.; Liu, N.; Fuller, E. J.; Agrawal, S.; Talin, A. A.; Li, Y.-Q.; Shen, B.-G.; Sun, Y. All-Solid-State Synaptic Transistor with Ultralow Conductance for Neuromorphic Computing. *Adv. Funct. Mater.* **2018**, 28, 1804170.

44. Tsuchiya, T.; Terabe, K.; Ochi, M.; Higuchi, T.; Osada, M.; Yamashita, Y.; Ueda, S.; Aono, M. *In situ* Tuning of Magnetization and Magnetoresistance in Fe_3O_4 Thin Film Achieved with All-solid-state Redox Device. *ACS Nano* **2016,** *10*, 1655-1661.

45. Namiki, W.; Tsuchiya, T.; Takayanagi, M.; Higuchi, T.; Terabe, K. Room-temperature Manipulation of Magnetization Angle, Achieved with an All-solid-state Redox Device. *ACS Nano* **2020**, *14*, 16065-16072.

46. Chiba, D.; Sawicki, M.; Nishitani, Y.; Nakatani, Y.; Matsukura, F.; Ohno, H. Magnetization Vector Manipulation by Electric Fields. *Nature* **2008**, *455*, 515−518.

47. Nakagawa, S.; Sasaki, I.; Naoe, M. Magnetization Processes of Storage and Back Layers in Double-Layered Perpendicular Magnetic Recording Media Observed Using Anomalous and Planar Hall Effects. *J. Appl. Phys.* **2002**, *91*, 8354−8356.

48. Bason, Y.; Klein, L.; Wang, H. Q.; Hoffman, J.; Hong, X.; Henrich, V. E.; Ahn, C. H. Planar Hall Effect in Epitaxial Thin Films of Magnetite. *J. Appl. Phys.* **2007**, *101*, 09J507.

49. Jin, X.; Ramos, R.; Zhou, Y.; McEvoy, C.; Shvets, I. V. Planar Hall Effect in Magnetite (100) Films. *J. Appl. Phys.* **2006**, *99*, 08C509.

50. Monalisha, P.; Li, S.; Bhat, S. G.; Jin, T.; Kumar, P. S. A.; Piramanayagam, S. N. Synaptic behavior of Fe_3O_4-based artificial synapse by electrolyte gating for neuromorphic computing. *J. Appl. Phys.* **2023**, *133*, 084901.

51. Miao, T.; Liu, W.; Huang, C.; Cui, B.; Chu, R.; Zhao, X.; Wu, X.; Wu, S.; Xie, J.; Liu, H.; Chen, J.; Cheng, B.; Hu, J. Multisensory synapses based on Fe_3O_4/graphene transistors for neuromorphic computing. *J. Mater. Chem. C* **2023**, *11*, 7732.

52. Margulies, D. T.; Parker, F. T.; Berkowitz, A. E. Magnetic Anomalies in Single Crystal Fe_3O_4 Thin Films. *J. Appl. Phys.* **1994**, *75*, 6097–6099.

53. Dho, J.; Kim, B.-G.; Ki, S. Distinctive Uniaxial Magnetic Anisotropy and Positive Magnetoresistance in (110)-Oriented Fe_3O_4 Films. *J. Appl. Phys.* **2015**, *117*, 163904.

54. Pacheco, A. F.; Orna, J.; De Teresa, J. M.; Algarabel, P. A.; Morellon, L.; Pardo, J. A.; Ibarra, M. R.; Kampert, E.; Zeitler, U. High-Field Hall Effect and Magnetoresistance in Fe3O4 Epitaxial Thin Films up to 30 Tesla. Appl. Phys. Lett., 2009, 95, 262108.

55. Lininger, C. N.; Cama, C. A.; Takeuchi, K. J.; Marschilok, A. C.; Takeuchi, E. S.; West, A. C.; Hybertsen, M. S. Energetics of Lithium Insertion into Magnetite, Defective Magnetite, and Maghemite. *Chem. Mater.* **2018**, *30*, 7922–7937.